AGU PUBLICATIONS

JGR

Journal of Geophysical Research: Atmospheres

RESEARCH ARTICLE
10.1002/2014JD022926

Key Points:
- Strong interannual variability of CO and aerosols on regional scales
- Biomass burning the main driver for CO, aerosols, OH, and partly for ozone
- Strong implications for air quality and climate forcing

Supporting Information:
- Figures S1–S3

Correspondence to:
A. Voulgarakis,
a.voulgarakis@imperial.ac.uk

Citation:
Voulgarakis, A., M. E. Marlier, G. Faluvegi, D. T. Shindell, K. Tsigaridis, and S. Mangeon (2015), Interannual variability of tropospheric trace gases and aerosols: The role of biomass burning emissions, *J. Geophys. Res. Atmos.*, *120*, 7157–7173, doi:10.1002/2014JD022926.

Received 30 NOV 2014
Accepted 17 JUN 2015
Accepted article online 18 JUN 2015
Published online 22 JUL 2015

Interannual variability of tropospheric trace gases and aerosols: The role of biomass burning emissions

Apostolos Voulgarakis[1], Miriam E. Marlier[2], Greg Faluvegi[3], Drew T. Shindell[4], Kostas Tsigaridis[3], and Stéphane Mangeon[1]

[1]Department of Physics, Imperial College London, London, UK, [2]Department of Ecology, Evolution, and Environmental Biology, Columbia University, New York, New York, USA, [3]Center for Climate Systems Research, Columbia University, and NASA Goddard Institute for Space Studies, New York, New York, USA, [4]Nicholas School of the Environment, Duke University, Durham, North Carolina, USA

Abstract Fires are responsible for a range of gaseous and aerosol emissions. However, their influence on the interannual variability of atmospheric trace gases and aerosols has not been systematically investigated from a global perspective. We examine biomass burning emissions as a driver of interannual variability of large-scale abundances of short-lived constituents such as carbon monoxide (CO), hydroxyl radicals (OH), ozone, and aerosols using the Goddard Institute for Space Studies ModelE composition-climate model and a range of observations, with an emphasis on satellite information. Our model captures the observed variability of the constituents examined in most cases, but with substantial underestimates in boreal regions. The strongest interannual variability on a global scale is found for carbon monoxide (~10% for its global annual burden), while the lowest is found for tropospheric ozone (~1% for its global annual burden). Regionally, aerosol optical depth shows the largest variability which exceeds 50%. Areas of strong variability of both aerosols and CO include the tropical land regions (especially Equatorial Asia and South America) and northern high latitudes, while even regions in the northern midlatitudes experience substantial interannual variability of aerosols. Ozone variability peaks over equatorial Asia in boreal autumn, partly due to varying biomass burning emissions, and over the western and central Pacific in the rest of the year, mainly due to meteorological fluctuations. We find that biomass burning emissions are almost entirely responsible for global CO interannual variability, and similarly important for OH variability. The same is true for global and regional aerosol variability, especially when not taking into account dust and sea-salt particles. We show that important implications can arise from such interannual influences for regional climate and air quality.

1. Introduction

Biomass burning (BB) emissions have been recognized as a major source of important atmospheric constituents such as carbon dioxide, carbon monoxide, nitrogen oxides (NO_x), and carbonaceous aerosols, among others [*van der Werf et al.*, 2010; *Voulgarakis and Field*, 2015]. Since several of those species interact with radiation, fires have been estimated to exert substantial radiative forcing of the climate from preindustrial times to present day and into the future [*Ward et al.*, 2012]. Fire emissions vary significantly on interannual timescales [*Duncan et al.*, 2003a; *van der Werf et al.*, 2010; *Huang et al.*, 2014], with tropical forests typically contributing more strongly than other types of ecosystems to this variability [*Randerson et al.*, 2005]. Therefore, fires may be playing an important role in the interannual variability (IAV) of trace gases and aerosols in the atmosphere, especially at its lower parts (troposphere).

One major mode of variability that is known to strongly affect global fire activity and, consequently, fire emissions, is the El Niño-Southern Oscillation (ENSO), which is a global climate fluctuation that originates from large-scale sea surface temperature (SST) anomalies over the tropical Pacific [*Philander*, 1990]. During the El Niño phase of ENSO (which can last for a year or more), the warm SSTs typically found over the western tropical Pacific are progressively displaced toward the eastern tropical Pacific, while during the La Niña phase, the opposite happens. The cooler SSTs over the western Pacific during El Niño lead to suppressed convection and rainfall, and thus drought, which favors the ignition of fires in the Maritime Continent [*Randerson et al.*, 2005]. The inverse occurs during La Niña, with the Maritime Continent experiencing conditions that do not favor fire activity, while South America being more prone to burning. An exceptionally dramatic case of an El Niño was that of 1997–1998, during which Indonesia experienced very intense burning with tremendous

amounts of pollution emitted into the atmosphere [*Duncan et al*., 2003b]. Important fire-related effects from El Niño also occur during less intense El Niño events, as was the case for 2006 [*Logan et al*., 2008]. Apart from its direct effects in the vicinity of the Pacific, ENSO can have significant effects on BB and pollution also in remote areas [*Spichtinger et al*., 2004; *Monks et al*., 2012], while it can also indirectly influence tropical tropospheric composition via modifications in the meteorology that affect the transport and chemistry of pollutants such as ozone and CO [*Oman et al*., 2013].

Some studies that have discussed BB effects on IAV have mainly focused on regional scales. For example, when it comes to CO, *Monks et al*. [2012] found that BB is the primary driver of its IAV over the Arctic, with ENSO being the underlying cause of the varying fire influence. *Mészáros et al*. [2005] found that the declining trend of carbon monoxide (CO) over Europe is occasionally interrupted due to strong fire emissions in other continents, while *Strode and Pawson* [2013] discussed how Siberian BB emissions can complicate trend detection in East Asian anthropogenic pollution. *Huang et al*. [2014] examined CO in the upper tropical troposphere and found that fire emissions from Indonesia during El Niño are a major IAV driver. A key global study by *Szopa et al*. [2007] suggested that meteorology is more important than BB emissions for driving CO IAV. However, its focus was solely on surface CO, while here we study the troposphere at its entirety, using satellite observations along with the modeling.

As is the case with CO, related studies for aerosols have mostly been regional. ENSO has again been associated with IAV of the tropical aerosol index, as was demonstrated by *Ji and Stocker* [2002]. *Habib et al*. [2006] found that fires are important for driving IAV in aerosol index over India. In the extratropics, *Spracklen et al*. [2007] found that BB is the major driver of IAV of surface carbonaceous aerosols over the western U.S. in the summer, while *Putero et al*. [2014] suggested that surface black carbon variability in the southern Himalayas is influenced by open vegetation fires. *Zhao et al*. [2012] examined the IAV of the aerosol loading in different seasons, but focusing on anthropogenically generated emissions from the northern midlatitudes. Important studies have used satellite information for detecting recent trends in aerosol abundances, but without discussing IAV [*Yoon et al*., 2014] or without exploring the role of fires in driving IAV [*Mu and Liao*, 2014]. The same is true for key studies investigating the IAV of global tropospheric ozone [*Hess and Mahowald*, 2009]; even some studies that did analyze the influence of BB only did it for a short period, with a more limited use of global observations in conjunction with the modeling [*Voulgarakis et al*., 2010], or focused only on a specific part of the globe [*Koumoutsaris et al*., 2008]. Regarding the other important tropospheric oxidant, namely, the hydroxyl radical (OH), BB emissions are expected to influence its IAV given that CO emissions can consume OH [*Dalsøren and Isaksen*, 2006], though more recent studies have actually suggested that global OH IAV may be minimal [*Montzka et al*., 2011].

In this paper, we extend the scope of the previous study by *Voulgarakis et al*. [2010] to explore the interannual variability of key short-lived tropospheric constituents that are of major importance for air quality and climate, namely, CO, ozone, hydroxyl radicals (OH), and tropospheric aerosols, and quantify the role of biomass burning as a driver. The past work provided valuable information on ozone and CO IAV, but here we study a longer time period (1997–2009), analyze additional species (global OH and aerosols), examine the role of BB emissions in particular, and use satellite and nonsatellite observations to constrain our model results. To our knowledge, this is the first study that examines the IAV of tropospheric composition and the role of BB systematically using both modeling and satellite observations and focusing on gases and aerosols simultaneously.

2. Methods

2.1. Model Description and Experimental Setup

We used the Goddard Institute for Space Studies (GISS) ModelE composition-climate model [*Shindell et al*., 2013; *Schmidt et al*., 2014], with a 2° latitude by 2.5° longitude horizontal resolution and 40 vertical layers from the surface to 0.1 hPa. The model's chemistry includes 156 chemical reactions among 51 gas species. Tropospheric chemistry includes basic NO_x-HO_x-O_x-CO-CH_4 chemistry as well as PANs and the hydrocarbons isoprene, alkyl nitrates, aldehydes, alkenes, and paraffins. The lumped hydrocarbon family scheme was derived from the Carbon Bond Mechanism 4 [*Gery et al*., 1989] and from the more extensive Regional Atmospheric Chemistry Model [*Stockwell et al*., 1997], following *Houweling et al*. [1998]. To represent stratospheric chemistry, the model includes chlorine- and bromine-containing compounds, and CFC and N_2O source gases (as well as an "age-of-air" passive tracer). As we use only a single CFC tracer, the ratio of

anthropogenic bromine to chlorine is held fixed at year 2000 values, with both released from CFC photolysis in an amount proportional to the total equivalent effective stratospheric chlorine loading in a given year. Photolysis rates are simulated using the Fast-J2 scheme [*Wild et al*., 2000; *Bian and Prather*, 2002], which accounts for the effects of modeled overhead ozone, clouds, aerosols, and surface reflections. The aerosol scheme includes prognostic simulations of the mass distributions of sulfate, sea salt, dust, and carbonaceous aerosols [*Koch et al*., 2006, 2007]. Secondary organic aerosol production depends on modeled isoprene and terpenes as oxidized by OH, ozone, and nitrate radicals [*Tsigaridis and Kanakidou*, 2007].

The model's skill in capturing key tropospheric gaseous constituents (e.g., CO and ozone which are studied here) and aerosols has been evaluated and shown to be realistic [*Koch et al*., 2006; *Voulgarakis et al*., 2011a; *Shindell et al*., 2013]. Also, the model has been thoroughly evaluated on its ability to capture ozone-CO correlations and slopes (which are metrics that indicate the model's ability to capture ozone-related processes in a variety of environments, including those impacted by BB [*Jaffe and Wigder*, 2012]) and has shown particularly good skill [*Voulgarakis et al*., 2011a]. Here, we will also discuss the model's ability to capture the IAV of important constituents on large scales.

We performed two 1997–2009 simulations (with two years of spin-up in advance): (a) BASE, which has interannually varying BB emissions and meteorology (via observed SSTs and nudging toward National Centers for Environmental Prediction reanalysis data), and (b) BBfix, in which 1997–2009 average BB emissions were repeated every year. Comparing BASE with BBfix will inform on the role of fires in driving IAV. BB emissions come from the Global Fire Emissions Database 3 (GFED3) [*van der Werf et al*., 2010] and were assumed to be uniformly mixed throughout the boundary layer. Anthropogenic emissions come from *Lamarque et al*. [2010] and vary from decade to decade, with linear interpolation for intermediate years. Biogenic isoprene emissions are a function of vegetation type and leaf area index with responses to temperature and solar radiation based on the algorithm of *Guenther et al*. [1995, 2006], while terpene emissions come from the output of the Organising Carbon and Hydrology In Dynamic Ecosystems model [*Lathiere et al*., 2006] and do not vary interannually. Lightning NO_x emissions depend on the climate model's convection based on the parameterization of *Price et al*. [1997]. Simulated trace gas and aerosol concentrations were not allowed to influence the model's radiation/climate. Well-mixed greenhouse gas concentrations vary according to global mean observed values.

2.2. Observations

We used a range of observational data sets to constrain the interannual variability found in our model, with an emphasis on satellite-derived information. The latter was our preference due to its relevance for global and large-scale regional tropospheric processes, which are the focus of our study.

For gases, we focus on CO and ozone information from the Tropospheric Emission Spectrometer (TES), a high-resolution (0.1 cm^{-1}), infrared, Fourier transform spectrometer aboard the NASA Aura satellite. The Aura satellite follows a polar Sun-synchronous orbit with an equator crossing time at 1:45 and 13:45 local time and has a repeat cycle of 16 days. TES covers a wide spectral range (650 to 3050 cm^{-1}) and has an averaged nadir footprint of about 5 km by 8 km [*Beer et al*., 2001]. The spectral radiances measured by TES are used to retrieve the species' (e.g., ozone and CO) mixing ratio profiles using the optimal estimation method [*Rodgers*, 2000; *Bowman et al*., 2002, 2006]. TES CO has been validated against aircraft data and has been shown to have a slightly negative (<10%) bias in midlatitudes and a slightly positive bias (<10%) in the tropics [*Luo et al*., 2007; *Lopez et al*., 2008]. TES ozone has been evaluated by comparison to ozonesondes [e.g., *Verstraeten et al*., 2013], aircraft data [e.g., *Richards et al*., 2008], and satellite data (Ozone Monitoring Instrument/Microwave Limb Sounder) [e.g., *Osterman et al*., 2008]. These studies show that TES ozone generally has a positive bias that varies between 2 and 7 ppbv [*Verstraeten et al*., 2013] in the troposphere.

In this study, we use version 6 TES global survey data for 2005–2009 (obtained from ftp://l5eil01.larc.nasa.gov/TES/), the period of our study for which TES obtained data. Each survey consists of observations from 16 full orbits. We have interpolated ozone and CO model output onto the 67 TES pressure levels for further processing. TES sampling and averaging kernels/a prioris have been applied to the 3-hourly model output. For plotting purposes, we have binned the observational and model IAV output onto a 4° latitude by 5° longitude grid in order to smooth out gaps in the observations (as in *Voulgarakis et al*. [2011a]).

For constraining modeled aerosol IAV, we used total aerosol optical depth (AOD) information from the Moderate Resolution Imaging Spectroradiometer (MODIS) [*Remer et al*., 2005] and the Multiangle Imaging

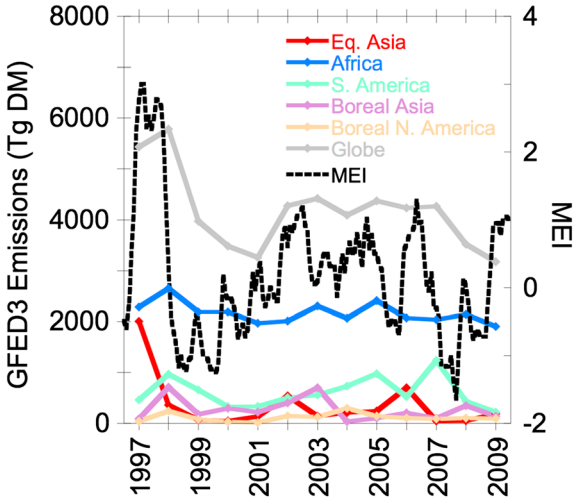

Figure 1. Annual mean dry mass fire emissions used in different regions (GFED3, *van der Werf et al.* [2010]) and monthly multivariate El Niño index (MEI) (http://www.esrl.noaa.gov/psd/enso/mei/#data) for the period of interest. For MEI, the *x* axis tick marks represent the middle of each year represented.

Spectroradiometer (MISR) [*Bull et al.*, 2009] onboard the NASA Terra satellite, which has an overpass time of 10:30 A.M. Since different satellite observations of AOD often show disagreements, we preferred to show results from two instruments rather than one. MODIS and MISR data have been found to typically have a correlation coefficient of 0.7 over land [*Kahn et al.*, 2009]. *Li et al.* [2014] also focused on Aerosol Robotic Network (AERONET) stations with long temporal records for comparison with MODIS and MISR satellite AOD observations and found strong spatial and temporal agreement between all data sets. AOD retrievals from MODIS take advantage of a wide spectral range, daily coverage of the globe, and high spatial resolution. Monthly mean Level 3 MODIS AOD information at 0.55 μm for both ocean (best) and land (corrected) at 1° × 1° horizontal resolution was used (data obtained from http://modis-atmos.gsfc.nasa.gov/MOD08_M3/), following interpolation onto a 2° latitude by 2.5° longitude grid (the GISS model's horizontal grid). Note that the MODIS version used here does not include retrieval over bright surfaces, such as the Sahara desert, the polar continents, and northern land mass during northern winter. MISR simultaneously observes the Earth at nine different angles and four spectral bands, with global coverage every 9 days at the equator. We used the gridded 0.5° × 0.5° Level 3 monthly AOD product (data obtained from https://eosweb.larc.nasa.gov/project/misr/version/pge12c) from the green (0.555 μm) band and interpolated onto a 2° × 2.5° horizontal grid, as was done for MODIS data. For comparing against MODIS and MISR with the model, we used clear-sky monthly mean model AOD corresponding to the visible band.

To complement our observational analysis, we have also used nonsatellite measurement data for CO, ozone, and aerosols from specific sites. We note that since our study is primarily focused on large-scale tropospheric processes and on exploiting satellite data and global modeling, we do not present an extensive analysis of the nonsatellite measurements. However, the information used is helpful for understanding the validity of the conclusions obtained from satellite observations. For CO, we compared against surface flask measurements from the NOAA Global Monitoring Division (GMD) Carbon Cycle Cooperative Global Air Sampling Network [*Novelli and Masarie*, 2010; ftp://ftp.cmdl.noaa.gov/data/trace_gases/co/flask/] for 47 sites (see Figure 9). For ozone, we used ozonesonde measurements from the World Ozone and Ultraviolet Radiation Data Centre (WOUDC) for 37 sites (http://beta.woudc.org/data/stations/). For aerosols, daily 500 nm AOD AERONET data [*Holben et al.*, 2001; http://aeronet.gsfc.nasa.gov/] were used from 44 stations. For comparisons to all the above specific site data, the 3-hourly model output was sampled according to the observation time and location. For ozone and CO, we restricted our analysis to stations that have data for at least 10 out of the 13 years in the 1997–2009 period that we study here. For AERONET, since data availability for some key regions was more restricted in terms of total years within 1997–2009, we reduced this threshold to 9 years instead of 10.

3. Results and Discussion

3.1. Gases

To have an idea of how the emissions that were input into our model varied in the period of interest, in Figure 1, we show the GFED3 total emissions of dry matter from fires (which are subsequently converted to emissions of specific species via the application of emission factors, see *van der Werf et al.* [2010]) for the whole globe as well as for some key regions, along with the multivariate El Niño index. It clearly shows that global fire emissions are well correlated with ENSO variations, typically with a small lag; for example,

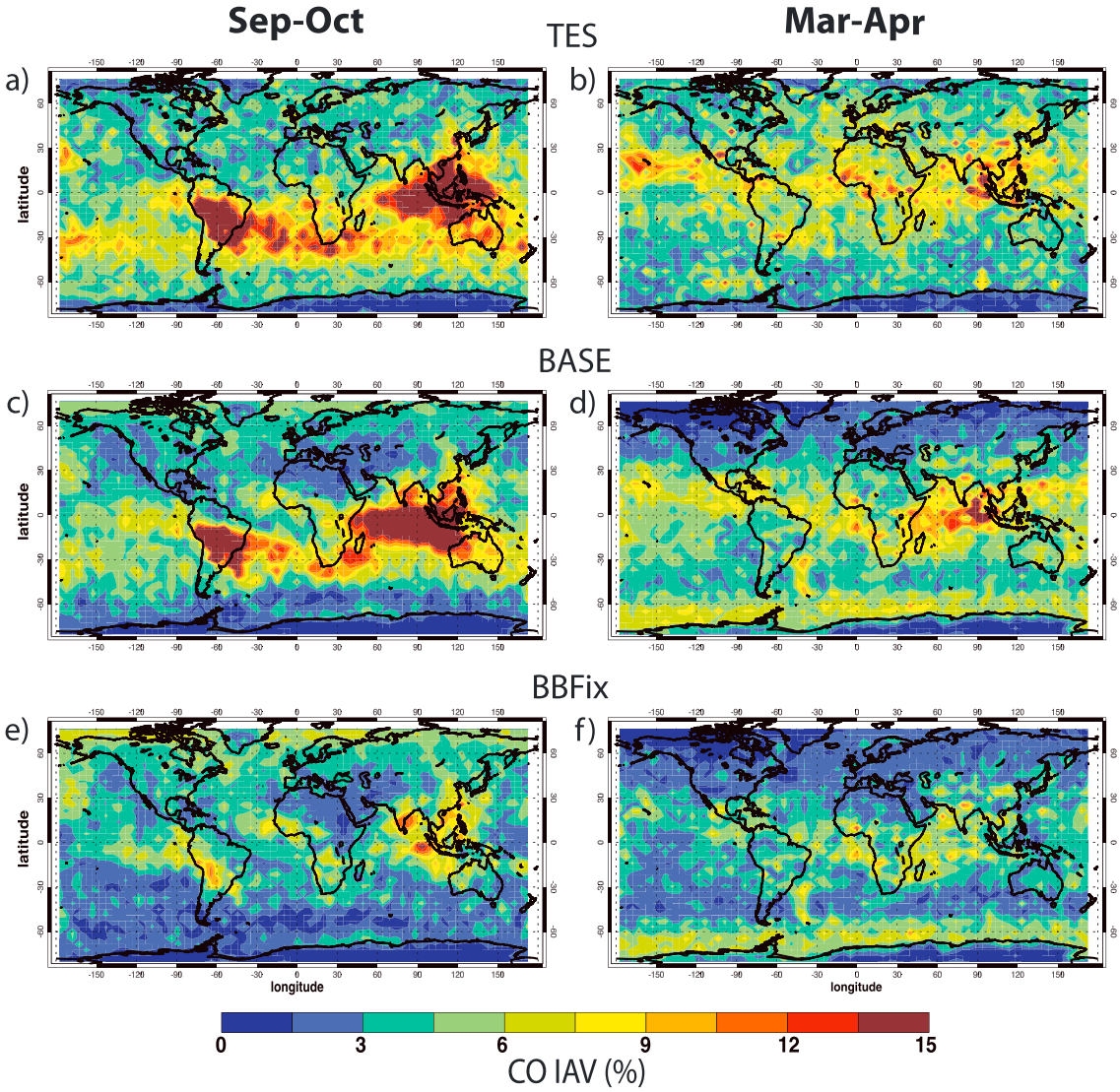

Figure 2. Tropospheric CO interannual variability (coefficient of variation) for September-October (left) and for March-April (right) between 2005 and 2009 from (a, b) the TES instrument, (c, d) the BASE simulation, and (e, f) the BBfix simulation. TES a priori profiles and averaging kernels have been applied to 3-hourly model output to produce these results. We averaged processed data from seven TES pressure levels between 800 and 400 hPa (the vertical region where TES is most sensitive) to create means for the middle/low free troposphere and calculate IAV. The data have been smoothed by averaging on a 4° × 5° grid before plotting.

the effect of the 1997–1998 El Niño is realized to its full extent in 1998, by when the dry conditions have had time to be established in key areas. The regions with the largest IAV in emissions are equatorial Asia and South America, with the values in those two regions being anticorrelated, since they experience drought in opposite phases of ENSO. African emissions are the largest in the globe in absolute terms but undergo smaller relative IAV. A significant contribution of emissions comes from boreal regions, with boreal Asia clearly experiencing stronger IAV in emissions than boreal North America.

Figure 2 shows the relative IAV as indicated by the coefficient of variation (CV, i.e., the multiyear standard deviation normalized by the mean) of free tropospheric carbon monoxide in September-October (hereafter, Sep-Oct) and March-April (hereafter, Mar-Apr), as observed by the TES satellite instrument (see section 2.2) and as simulated by the model, for the 5 years of the simulation for which TES observations are available (2005–2009). We chose these seasons as they correspond to the times of the year when fire activity peaks in equatorial Asia (basically, the Maritime Continent), South America, and parts of Africa south of the equator (Sep-Oct), as well as in parts of Africa north of the equator and in Southeast Asia (Mar-Apr) [*van der Werf et al.*,

2010]. Furthermore, Northern Hemisphere (NH) spring is the time of the year when both CO and ozone at remote sites over northern midlatitudes peak [*Zbinden et al*., 2013]. The model's ability to capture free tropospheric CO and ozone for the same years has been evaluated in *Voulgarakis et al*. [2011a] and shown to be good, both in terms of broad geographical patterns and in terms of mean concentration levels.

The largest IAV by far is seen for Sep-Oct (Figure 2a). The areas that stand out as hot spots of variability in the observations are primarily tropical areas, and especially equatorial Asia and South America. Since both these regions are known to experience intense BB activity, this feature immediately suggests that the IAV observed may be due to BB (to be examined further later). The model output captures remarkably well both the location and the magnitude of CO IAV maxima (Figure 2c). For Mar-Apr (Figure 2b), observed CO IAV is generally much smaller than in Sep-Oct. There are no major hot spots of IAV, though areas of Africa around/north of the equator and Southeast Asia stand out, which is consistent with the peak in fire activity that occurs at this time of the year in these regions. Still, the CO IAV found in Africa in both seasons and in Southeast Asia in Mar-Apr is much smaller than that found in and around other tropical land regions, such as equatorial Asia and South America, in Sept-Oct. The model manages to capture the Mar-Apr CO IAV hotspots in Southeast Asia/Indian Ocean and Africa, though with somewhat less pronounced magnitude in the latter region.

We also examined the two other seasons (Figure S1, supporting information), namely, NH summer (Jul-Aug) and winter (Dec-Jan), of which none showed as strong IAV features as Sep-Oct. However, the hot spots in Jul-Aug (Figure S1a) and Sep-Oct (Figure 2a) are located in similar areas within the tropics, that is, South America, equatorial Asia, and Africa, with the two former featuring much less IAV than in Sep-Oct. We note though that with a plotting color scale that has a substantially lower maximum, the features in these regions start becoming more similar to Sep-Oct (not shown). Another important difference between Jul-Aug and Sep-Oct is that in the former there is some pronounced CO IAV over boreal regions, especially Siberia and North America. Boreal regions experience more fire activity in the NH summer, so this observational feature indicates that fire activity could be the reason for pronounced CO IAV in these regions in Jul-Oct. In NH winter (Dec-Jan; Figure S1b), there is some pronounced observed CO IAV in parts of central Africa and South America, but generally IAV is small. In these two seasons (Jul-Aug and Dec-Jan), the model captures reasonably well the minor tropical IAV hot spots (Figures S1c and S1d), though it misses the local maximum over South America in Dec-Jan. In the extratropics, a systematic feature of the model-satellite comparison is that the model tends to show too small a CO IAV in northern midlatitudes/high latitudes, both in the NH fire season (Jul-Aug) and in other seasons.

We compare the results from the BASE model run with BBfix, in order to isolate the role of BB emissions in driving the IAV of CO. From comparing Figures 2c, 2d, and S1c with Figures 2e, 2f, and S1e, respectively, it is evident that the IAV of CO is drastically decreased when removing the IAV in BB emissions. This is especially true for the equatorial/Southeast Asia and South America (in line with maximum IAV in emissions as found by *Randerson et al*. [2005] and shown in Figure 1). For Africa, there is still substantial IAV in the BBfix run (especially in Dec-Jan), which is most likely due to meteorological variability, leading to changes in the amount of pollution exported from the region from year to year [*Huang et al*., 2014]. The same is true for boreal regions in the local fire season (Jul-Aug). Interestingly, for Jul-Aug, there is more IAV over Africa in BBfix compared to BASE, which is likely due to the fact that there are meteorological effects on CO in the region that in the BASE run are masked by the coinciding fluctuations in BB emissions.

We performed a similar analysis for the IAV of tropospheric abundances of ozone (Figures 3 and S2). The geographical distribution of relative IAV only has major similarities to that of CO in Sep-Oct, which suggests that the large signal from BB emissions IAV in that season may also play a role in driving ozone IAV. In other seasons, the western and central Pacific stand out as the hot spots of ozone IAV. Notably, these were also the hot spot areas in terms of ozone-CO correlations in a previous study by *Voulgarakis et al*. [2011a]. This strong ozone IAV could be explained by the large interannual variations in meteorological conditions in the area, as driven by ENSO [*Lin et al*., 2014]. The latter not only affects BB intensity over the Maritime Continent but also drives changes in the vertical and horizontal transport of ozone precursors in the region, as well as variations in ozone production and loss processes as driven by humidity and radiation changes [*Voulgarakis et al*., 2010; *Oman et al*., 2013]. We also note that in the northern extratropics, observed ozone IAV is maximum in Mar-Apr and minimum in Jul-Aug. The NH spring maximum IAV is possibly a consequence of the maximum input of

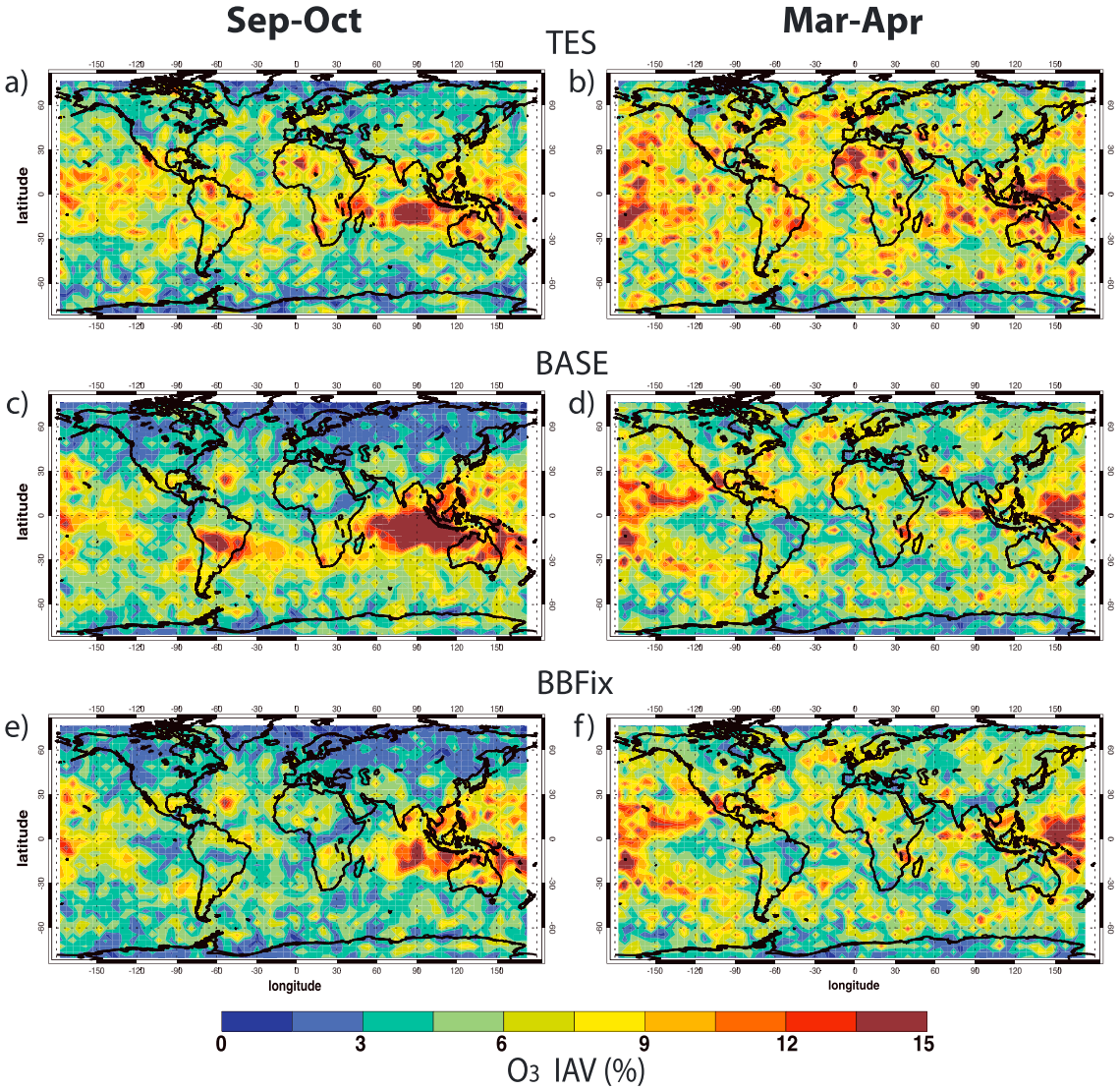

Figure 3. Tropospheric ozone interannual variability (coefficient of variation) for September-October (left) and for March-April (right) between 2005 and 2009 from (a, b) the TES instrument, (c, d) the BASE simulation, and (e, f) the BBfix simulation. TES a priori profiles and averaging kernels have been applied to 3-hourly model output to produce these results. We averaged processed data from seven TES pressure levels between 800 and 400 hPa (the vertical region where TES is most sensitive) to create means for the middle/low free troposphere and calculate IAV. The data have been smoothed by averaging on a 4° × 5° grid before plotting.

stratospheric ozone into the midlatitude troposphere in that season [*Zbinden et al.*, 2013], which is a process undergoing substantial IAV, largely driven by ENSO as suggested by previous studies [*Zeng and Pyle*, 2005; *Voulgarakis et al.*, 2010, 2011b; *Neu et al.*, 2014].

Most of the key seasonal and geographical ozone IAV features mentioned above are also well captured by the model, though in the peak tropical BB season (Sep-Oct), the model tends to have too strong tropical IAV. By comparing BASE to BBfix (Figures 3c, 3d, S2c, and S2d to Figures 3e, 3f, S2e, and S2f, respectively), it is evident that BB emissions are important for ozone IAV mainly in Sep-Oct over equatorial Asia and South America, and even in that case, not completely. For equatorial Asia, the BB effects are evident more in the middle of the BB activity region (comparison of Figures 3c and 3e over Indonesia), while in surrounding areas, the IAV remains high in BBfix. As discussed above, the ENSO-driven meteorological fluctuations (especially in transport processes) from year to year tend to drive this remaining variability [*Voulgarakis et al.*, 2010]. For seasons outside of NH autumn and regions other than equatorial Asia, the BB effects on tropospheric ozone are minimal. For the Pacific area of relatively high ozone IAV, our results show that BB emissions do not play a

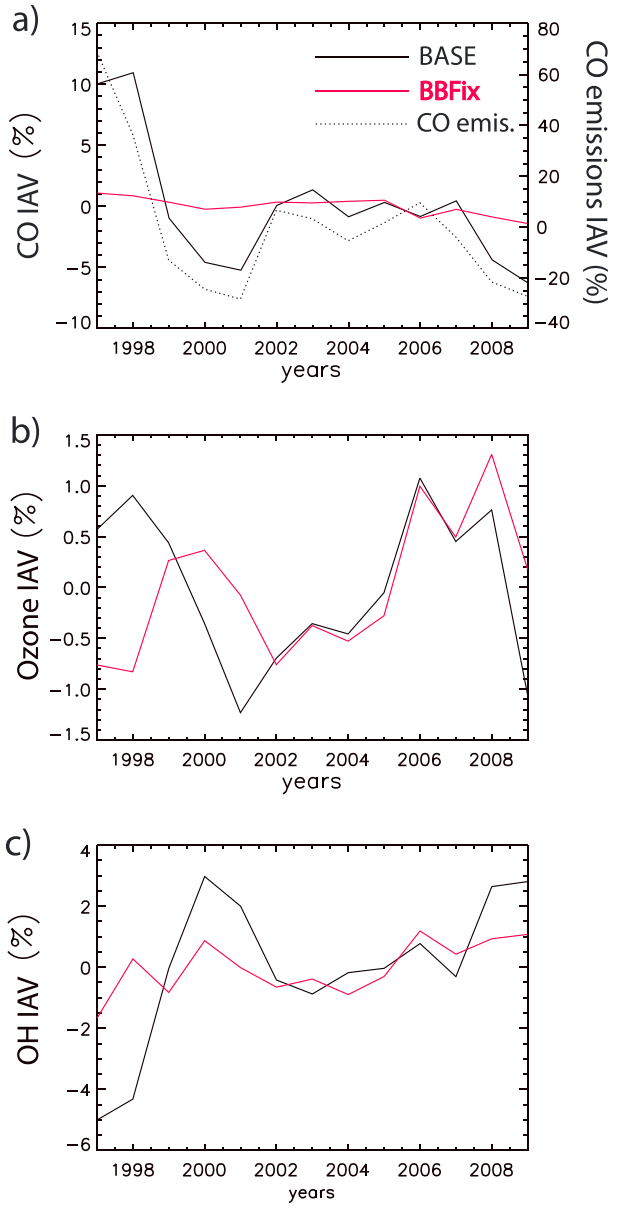

Figure 4. Percentage deviations (%) from the 13 year mean for global annual tropospheric (a) CO burden, (b) ozone burden, and (c) mass-weighted mean OH concentration for the BASE (black) and BBfix (red) simulations. Overplotted in Figure 4a are the global total CO fire emissions (dotted). Model output data for 1997–2009 were used. The tropopause was assumed to follow the 150 ppbv ozone surface. No TES processing was applied to model data here.

major role, which is in agreement with the recent study by *Lin et al.* [2014] who found that meteorological variability and specifically the strength and location of the subtropical jet and associated long-range transport of Asian pollution was much more important for driving ozone IAV at the Mauna Loa Observatory, at least for NH spring.

Figure 4a shows the relative IAV of the global annual tropospheric burden (GTB) of CO for the period of study, in the BB and BBfix simulations. CO GTB shows large IAV, of the order of ±10%, which is remarkable for a global quantity. It is noteworthy that during all the El Niño events included within the period of study (1997–1998, 2002–2003, 2004–2005, and 2006–2007), global CO shows a tendency to be higher, while during all the La Niña events (1999–2000, 2000–2001, 2005–2006, 2007–2008, and 2008–2009), it shows the opposite tendency. The strongest increases/decreases occur in the strongest and more prolonged El Niño/La Niña cases between 1997 and 2009, namely, 1997–1998 and 2002–2003 (El Niño) and 1999–2000 and 2007–2008 (La Niña).

We find that BB emissions, and not the secondary CO chemical production or the meteorological variability, is the overwhelmingly dominant factor driving IAV in global tropospheric CO, as when fixing BB emissions, global CO fluctuations almost disappear (Figure 4a). The dominant role of emissions in general in driving large-scale CO IAV was also discussed in the previous study by *Voulgarakis et al.* [2010], performed with a different model and using fewer years. In contrast, *Szopa et al.* [2007] suggested that meteorology is the dominant CO IAV driver in the tropics and an important driver in the extratropics. However, their conclusions come mainly from comparing their model against surface measurement data, which are more easily affected by local meteorology and are not representative of the large-scale total tropospheric burden. More discussion of the difference between IAV of CO when calculated from surface concentrations versus large-scale burdens is provided in section 3.3.

We note here that the estimated CO and ozone variability from the TES observations, as well as from the model following application of TES operators, may be an underestimate of what happens in reality. This is due to the fact that when the sensitivity of the instrument is low (primarily in scenes that are obscured by clouds), both TES and processed model values revert to the assumed a priori profile, which does not vary from

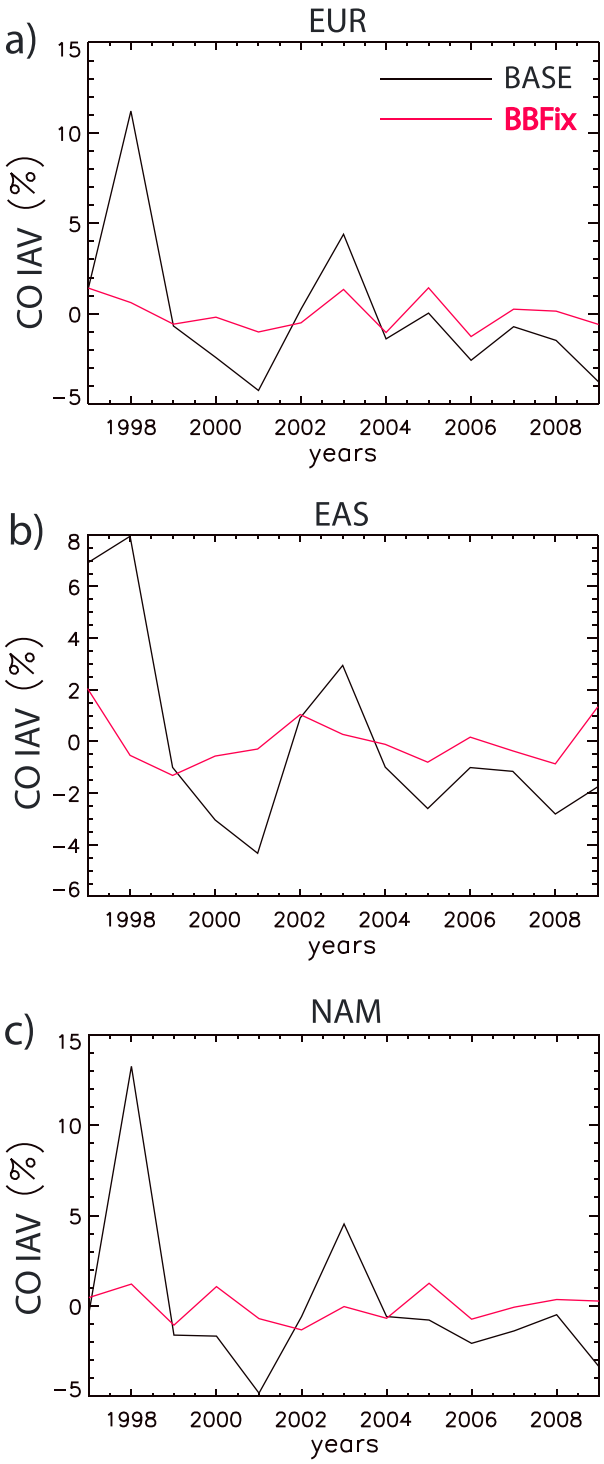

Figure 5. Percentage deviations (%) from the 13 year mean for regional annual tropospheric CO burden for (a) Europe (10°W–35°E, 34–54°N), (b) East Asia (110–140°E, 20–45°N), and (c) temperate North America (124–70°W, 34–54°N). Model output data for 1997–2009 were used. The tropopause was assumed to follow the 150 ppbv ozone surface. No TES processing was applied to model data here.

year to year [e.g., *Voulgarakis et al.*, 2011a]. For example, in northern midlatitude regions such as Europe, East Asia, and North America, for which the CO IAV values in Figures 2 and S1 are relatively low, if we construct IAV plots with unprocessed raw model data (Figure 5), the variability appears substantially larger than in Figures 2c and 2d or S1c and S1d. As is the case for the global case (Figure 4a), BB appears to be the major factor driving CO IAV in those individual regions (Figure 5). Attributing this regional CO IAV to local or remote BB emissions would require further sensitivity simulations. However, the fact that the regional CO time series in Figure 5 correlate well with the time series of global CO BB emissions (Figure 4a), which, in turn, are driven largely by either tropical or boreal high-latitude burning, indicates that the drivers are most likely nonlocal and stresses the importance of long-range transport of pollution.

The IAV of global aggregated abundances of the most important tropospheric oxidants, namely, ozone and hydroxyl radicals, is shown in Figures 4b and 4c. In contrast to CO, the IAV of the ozone GTB is very small in magnitude (around ±1%), which is in line with the understanding that the global tropospheric ozone abundance is fairly well buffered [*Wild and Palmer*, 2008]. The areas found earlier to have the strongest ozone variability (e.g., the tropical Pacific and Indian Oceans; Figures 3 and S2) are at the same time locations with low absolute ozone abundances, and therefore, they do not influence the global ozone burden substantially. Our global ozone IAV, however, is significantly lower than that found in previous studies using a different model [*Voulgarakis et al.*, 2010, 2011b]. The role of BB in driving global ozone IAV in our model varies depending on the period: between 1997 and 2001, it is an important factor, with the IAV being different in BASE and BBfix, while between 2002 and 2009, BB influence is minimal. This may imply that BB emissions can influence ozone IAV globally mainly in cases of extreme El Niño events, like in the 1997–1998 case, as well as in the subsequent La Niña period.

Note that for the 1996–2000 period, *Voulgarakis et al*. [2010] found that total emissions were responsible for 11% of global tropospheric ozone IAV, but without separating the role of BB. The major driver of global ozone variability was found to be meteorology, and especially the influence of ENSO on large-scale dynamical variability and on the influx of ozone-rich air from the stratosphere [also see *Zeng and Pyle*, 2005]. Note that meteorology has also been found to be a major factor driving NO_x IAV [*Uno et al*., 2007; *Savage et al*., 2008; *Voulgarakis et al*., 2010], which we do not study here. However, for NO_x, which have a shorter lifetime than ozone, stratosphere-troposphere influences are less important than transport processes that occur within the troposphere, especially on regional scales.

For global mean OH (Figure 4c), IAV is nonnegligible (about ±4–5%), but relatively small, and similar to recent observational estimates [*Montzka et al*., 2011] or to the IAV typically inferred from global models [e.g., *Dalsøren and Isaksen*, 2006]. By comparing Figure 4c with Figure 4a, it is evident that OH variability is strongly anticorrelated with that of CO ($R = 0.98$), suggesting that OH loss via CO oxidation is the major driver of global OH IAV. Also, by comparing BASE and BBfix for OH, it is evident that BB emissions are a major driver of modeled global OH IAV. ENSO variability again appears as the major driver, with El Niño years featuring low global OH (due to high CO) and La Niña years featuring high global OH (due to low CO).

3.2. Aerosols

Figures 6 and S3 show the geographical distribution of the IAV in the total AOD (dominated by the tropospheric aerosol abundances). For NH summer and autumn (Figures 6a and S3a), retrievals from MODIS (see section 2.2) between 2000 and 2009 show similar tropical hot spots of IAV as for CO, with South America and equatorial Asia standing out. Also, the areas of high AOD variability in the boreal regions are more extensive than in the case of CO, and the hot spot areas even include parts of midlatitude regions such as the U.S. and Europe. The maximum regional variability in AOD is also much higher than for CO, with some areas experiencing higher than 50% IAV (though note the influence of a priori profiles on the IAV shown in Figures 2, 3, S1, and S2, which may be leading to CO and ozone IAV underestimates, as discussed earlier). Interestingly, the IAV in Africa is much smaller than in the other tropical regions, possibly reflecting that the strong influence of ENSO-driven meteorological variability directly affects the Maritime Continent and South America, but not Africa. *van der Werf et al*. [2010] showed that grassland and savanna fires have a coefficient of variation (CV) of 11% in the 1997–2009 GFED3 data set, while the CV of peat fires was 176%, in line with our findings. Our Figure 1 also shows that for Africa the relative variability of emissions is smaller than in other tropical regions. However, since that IAV is not totally negligible, we cannot rule out the possibility that simultaneous meteorological effects may be dampening the influence of BB emissions. This issue is worth investigating in future work.

In Figures 6c and S3c, we show IAV results from the MISR satellite instrument for Sep-Oct and Jul-Aug. Generally, MISR and MODIS are in agreement here when it comes to the hot spots of aerosol IAV for these seasons, even for the somewhat unexpected features of much more widespread hot spots of variability in boreal regions compared to CO and of weak variability over Africa, which enhances confidence in our conclusions. However, there is a systematic tendency for MISR to show somewhat less strong IAV than MODIS. As was the case for CO, the model captures IAV hot spots well, though with significant and often large underestimates of IAV over boreal regions (Figures 6e and S3e). There is also a notable strong discrepancy over Australia between the model and MODIS IAV for all seasons, though this comparison is inconclusive, since MODIS and MISR give largely different IAV in this region. Another similarity with CO is that also here BB appears to be the major driver of IAV (Figures 6g, 6h, S3g, and S3h). The only exception is the western Pacific, east of the Maritime Continent, where IAV presumably is mainly driven by the variability of transport processes related to ENSO that export pollution from neighboring regions (also discussed by *Voulgarakis et al*. [2010], for gaseous pollutants); however, this relative variability is associated with fairly low absolute AOD values that typically occur in this region.

In NH winter and spring (Dec-Jan and Mar-Apr), MODIS and MISR do not agree as well when it comes to IAV, especially over Australia and equatorial Asia. More agreement between the instruments is found over South America and the Southern Ocean, though those features are nonexistent or much weaker in the model. The few areas with substantial IAV in BASE still appear in BBfix, which suggests that during NH winter and spring BB emissions are not an important driver of AOD IAV (an exception is the high-IAV spot over northeast Asia in Mar-Apr). However, due to the instrument disagreements mentioned above, this result is less conclusive. Further study of tropospheric aerosol IAV is needed with different models to confirm this

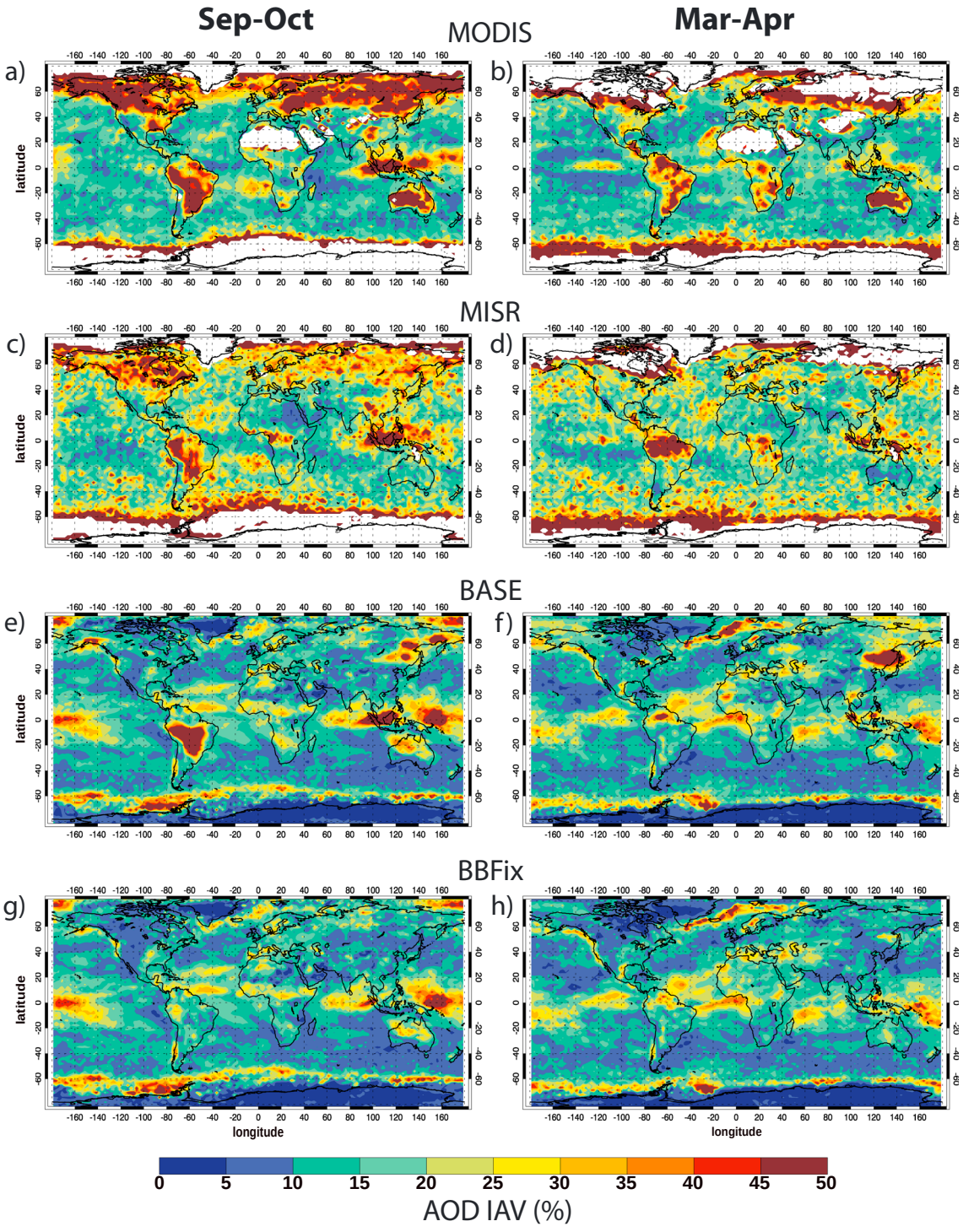

Figure 6. Total aerosol optical depth (AOD) interannual variability (coefficient of variation) for July-August (left) and December-January (right) from (a, b) the MODIS instrument, (c, d) the MISR instrument, (e, f) the BASE simulation, and (g, h) the BBfix simulation. Data from the 2001–2009 period were used. Only clear-sky values were taken into account from the model output. Note that the MODIS version used here does not include retrieval over bright surfaces, such as the Sahara desert, the polar continents, and northern land mass during northern winter.

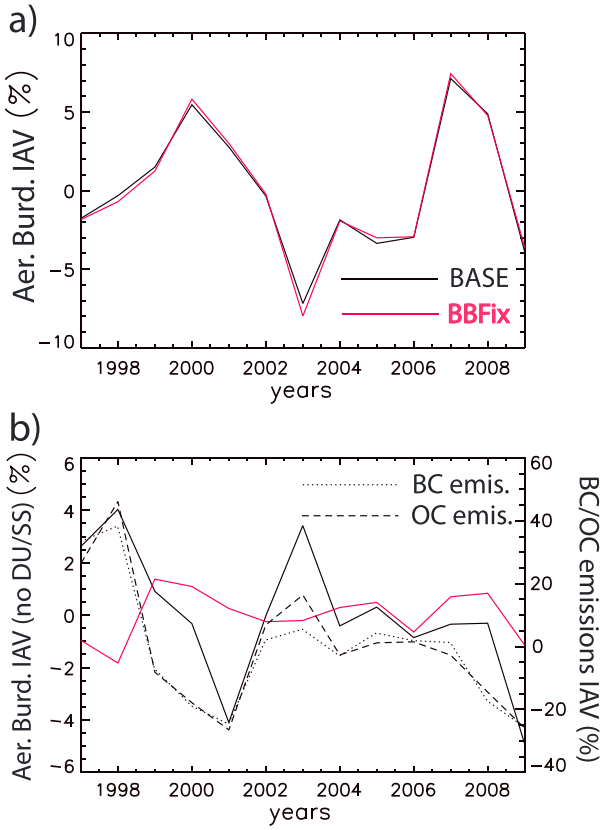

Figure 7. Percentage deviations (%) from the 13 year mean for global annual tropospheric (a) aerosol burden and (b) aerosol burden excluding dust and sea salt. Overplotted in Figure 7b are the global total BC (dotted) and OC (dashed) fire emissions. Model output data for 1997–2009 were used. The tropopause was assumed to follow the 150 ppbv ozone surface.

key result (i.e., aerosol IAV being smaller in NH winter/spring). A relevant past study examined aerosol IAV in different seasons and actually found larger IAV in the winter [*Zhao et al.*, 2012] but had considered only IAV in aerosols from anthropogenic northern midlatitude sources and not from BB.

Figure 7a shows the IAV of the GTB of aerosols, which includes all of the aerosol tracers simulated in the model. It is clear that BB emissions are not an important driver of the IAV in the total mass of aerosols in the troposphere. However, the total aerosol mass is dominated by coarse particles such as sea salt and dust. When we remove those types of primarily natural aerosols from the calculation, BB emerges as an important driver of global aerosol IAV (Figure 7b). The BB effect is even stronger when considering the nondust/nonsea-salt global aerosol burden below 850 hPa (not shown), where we find BB emissions to be overwhelmingly the major driver of IAV, similar to global CO. We note that, as for CO, the GTB of aerosols shows a clear tendency to be higher during El Niño years and to decrease during La Niña years.

In Figure 8, we briefly examine some key implications of the interannual variations that we discuss. We examine the IAV of annual mean aerosol radiative effect (RE) and surface aerosol pollution in the model. We focus on the instantaneous RE by black carbon aerosols, which are one of the major aerosol species emitted from fires. It is clear that, similar to the column AOD, large IAV is found in regions such as the Maritime Continent, South America, and boreal regions. Such strong fluctuations (in some cases exceeding 50%) are expected to have implications for year-to-year climate variability in those regions. We also show that BB emissions are responsible for these variations in RE (Figure 8c), which indicates the major role of fires in the climate systems of both tropical and boreal regions. Note that for the other important type of carbonaceous aerosols, that is, organic carbon, the RE IAV features are very similar, with somewhat more extensive hot spot areas over boreal regions. Figure 8b shows the IAV in annual mean $PM_{2.5}$ (aerosol particles with diameters less than 2.5 μm), with similar hot spots as for RE and a similarly large role of BB emissions. Therefore, it is clear that fires can drive very large fluctuations in surface air quality levels even in highly populated regions (e.g., Indonesia and Brazil), something that can have important implications for population health [*Marlier et al.*, 2013].

3.3. Comparison to Nonsatellite Observations

Our analysis is primarily focused on satellite information, which is suitable for understanding large-scale processes examined in this study. Here we complement our analysis with a short comparison of modeled constituent IAV to nonsatellite observations. Specifically, we have compared the model's output against GMD CO, WOUDC ozone, and AERONET AOD (see section 2.2 for details regarding the nonsatellite data sets used), which are global networks with a large geographical spread of stations (see Figure 9 for exact locations of stations used). The results of the comparison of modeled to observed IAV are shown in Table 1.

For CO, information on a global scale is only available from the surface (when it comes to nonsatellite data), with the main source being the GMD network. According to the observations, the strongest IAV for surface

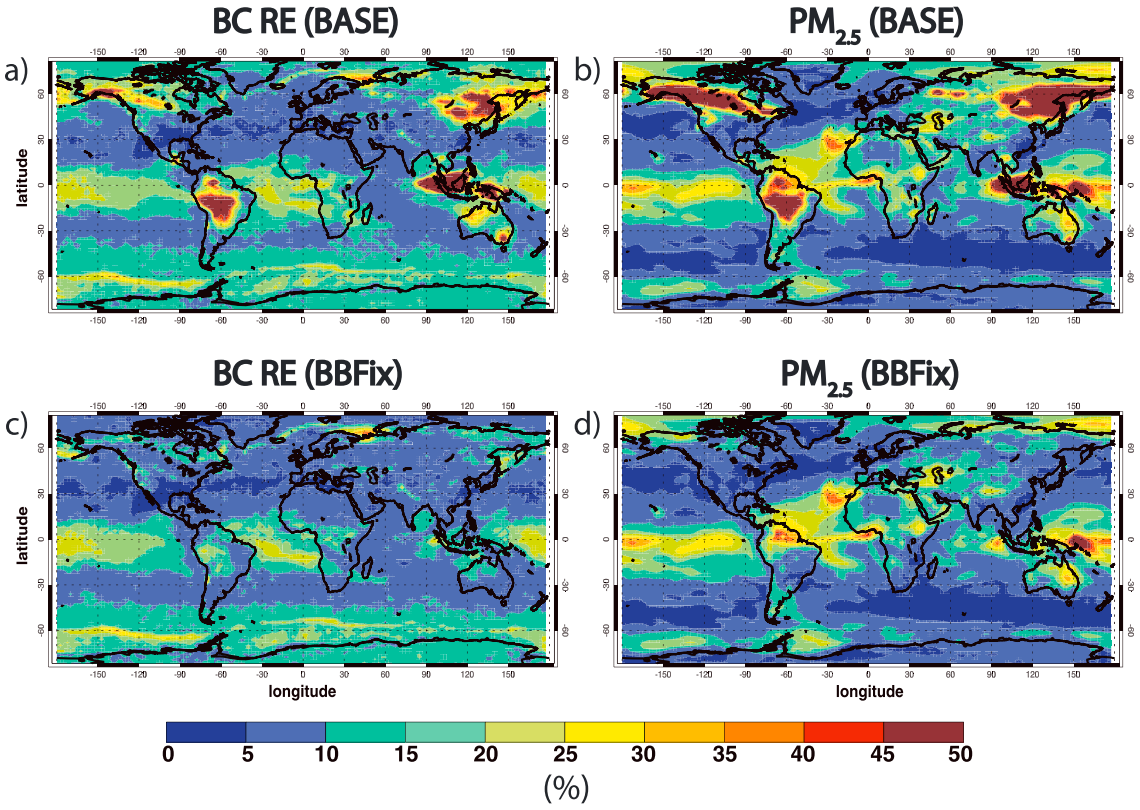

Figure 8. Annual mean black carbon (BC) instantaneous top-of-the-atmosphere radiative effect (RE) and surface $PM_{2.5}$ concentration interannual variability (coefficient of variation) from (a, b) the BASE simulation and (c, d) the BBfix simulation. Data from the 2001–2009 period were used. For RE, only clear-sky values were taken into account from the model.

annual mean CO is found in tropical regions, as well as in the Southern Hemisphere extratropics (SHXT). Our model agrees with the magnitude of IAV over Africa and the tropical Pacific islands but underestimates the IAV over South America and the SHXT. However, we note that none of the two GMD stations in South America that had enough years of data for our analysis is located in or near the Amazon, which was the part of South

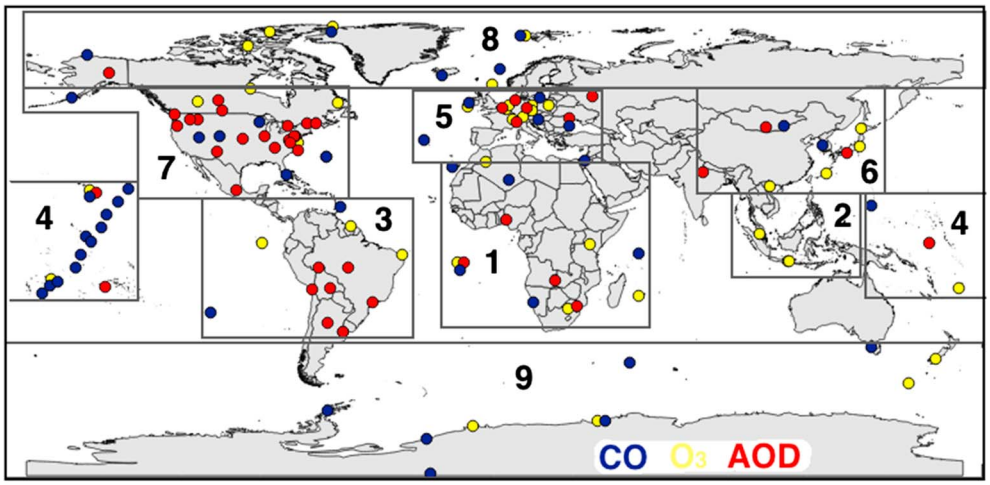

Figure 9. Nonsatellite observational sites used in our analysis: GMD CO (blue), WOUDC ozonesonde (yellow), AERONET AOD (red). The rectangles overplotted indicate the regions referred to in Table 1: (1) Africa, (2) equatorial Asia, (3) South America, (4) tropical Pacific islands, (5) Europe, (6) East Asia, (7) North America, (8) Arctic, and (9) Southern Hemisphere extratropics.

Table 1. Interannual Variability (Coefficient of Variation in Percent) in Model Simulations and Nonsatellite Observations for the 1997–2009 Period[a]

	CO (BASE)	CO (BBfix)	CO (Obs.)	O3 (BASE)	O3 (BBfix)	O3 (Obs.)	AOD (BASE)	AOD (BBfix)	AOD (Obs.)
AFRICA	12.6	11.9	12.9	3.9	2.4	6.8	23.3	19.9	22.5
EQ ASIA	-	-	-	5.7	3.5	11.1	-	-	-
S AMER	6.3	6.6	10.5	3.2	3.8	5.1	32.5	23.5	26.6
PACIFIC	19.4	15.3	15.5	7.1	6.8	5.9	20.4	20.7	14.0
EUROPE	6.0	5.0	11.2	2.2	1.9	2.2	13.0	15.0	18.4
E ASIA	5.6	5.8	8.3	2.4	1.6	4.2	14.5	13.8	16.3
N AMER	10.4	8.5	8.5	2.8	1.8	2.7	13.9	13.6	24.8
ARCTIC	15.1	7.0	8.1	3.3	2.2	3.7	57.1	16.6	66.5
SHXT	5.4	3.8	11.0	2.7	2.8	3.3	-	-	-

[a]Annual regional means were used for these calculations. For CO, we use surface observations and output for the lowest model level. For ozone (O_3), we show results from the comparison at 500 hPa. The definition of the regions can be seen in Figure 9. "S AMER" stands for "South America," and similarly for North. "SHXT" refers to the Southern Hemisphere extratropics. "PACIFIC" refers to tropical Pacific islands.

America with the strongest IAV in satellite observations. Unfortunately, there were no data with enough years from Southeast Asia, which is a key area of our study. When it comes to the role of BB emissions, the only regions where it appears strong (compare CO BASE with CO BBfix columns) are the Arctic and (less) North America, while in the rest of the regions, its effect is smaller. These results are in agreement with the findings of *Szopa et al*. [2007], who suggested that meteorology is much more important than emissions in driving tropical surface CO IAV, while in the extratropics, BB emissions also become important (though not dominant). The fact that GMD information is for the surface, however, makes the CO IAV results shown in Table 1 not directly comparable to the results obtained from our comparison to satellite information earlier in the manuscript. As mentioned before, surface CO concentrations are more easily affected by local meteorology and are not representative of the large-scale total tropospheric burden.

For annual mean ozone, we compare model output with WOUDC ozonesonde observations at 500 hPa, as this is a height that is representative of the middle free troposphere, on which we are also focusing in the satellite analysis. In agreement with our findings from the comparison against TES, the region with the highest IAV is equatorial Asia, while the neighboring region of the tropical Pacific is also an area of strong IAV, as we found earlier. Even though those two regions also show the highest IAV in the model, the latter underestimates IAV in equatorial Asia, which was also the case in the comparisons against TES for Mar-Apr/Dec-Jan, but not in the rest of the year. Lower ozone IAV is found in midlatitude and high-latitude regions. The comparison against ozonesondes also agrees with the satellite comparison on the fact that BB emissions have the strongest effect on ozone IAV in equatorial Asia, while in the rest of the globe, their effects are smaller.

Our comparison with AERONET AOD first of all confirms the higher IAV for aerosols than for CO and ozone that were found in the satellite instruments and in the model. For all the regions in Table 1 (note the lack of sufficient information for equatorial Asia), the IAV of annual AOD is higher than 10%, with the highest IAV found in the Arctic (66.5% in the observations and 57.1% in the model). The northern midlatitude and high-latitude AOD IAV is generally underestimated, as was also found from the satellite analysis. In South America, the model overestimates IAV compared to AERONET, which implies that the overestimates that we found earlier in Sep-Oct and Jul-Aug are more important for the annual mean than the underestimates found in the other seasons. Again in agreement with our earlier results, the AERONET comparison with the model shows that BB emissions are key in driving the IAV in areas with high-amplitude AOD variability such as South America and boreal regions (Arctic), while in Africa, their effects are smaller though still present.

Overall, we conclude that our analysis against nonsatellite observational information confirms the results from our analysis using satellite data for AOD and tropospheric ozone.

4. Conclusions and Discussion

We show that biomass burning emissions can be an important driver of global tropospheric composition interannual variability, with particularly strong effects for important constituents such as CO and aerosols, and nonnegligible effects for OH. These species are key as they exert major influences in processes that

are related both to climate and to air pollution, and so these findings suggest how and where biomass burning emissions can affect the variability of large-scale air quality as well as radiative forcing. We also used satellite observations to evaluate the NASA GISS global composition-climate model in how it captures the IAV of tropospheric constituents and found that its performance is good, though with underestimates of IAV in boreal regions both for CO and for aerosols. There is the possibility that the fire emissions used might be causing this disagreement, rather than the model processes themselves. Even though it has been shown that the GFED3 burned area estimates are fairly good in boreal regions [*Giglio et al*., 2010], there are relatively large uncertainties in inferred emissions in boreal regions due to difficulties in estimating how much the organic soils burn [*van der Werf et al*., 2010]. We note though that such biases are not expected to have large impacts on the global burdens examined here, given that boreal Asia and North America contribute only around 9% of global fire emissions (see Figure 1 and *van der Werf et al*. [2010]).

Our study does not fully account for IAV in anthropogenic emissions, as the *Lamarque et al*. [2010] data set only provides decadal emissions with interpolation in between years. However, we expect that anthropogenic emissions do not vary on interannual timescales sufficiently in order to compete with the BB emissions when it comes to atmospheric composition effects. For example, in the Reanalysis of the Tropospheric Chemical Composition Over the Past 40 Years project's emission data set [*Schultz et al*., 2008], which provides estimates of interannually varying anthropogenic emissions, the relative variability of global detrended CO emissions between 1991 and 2000 (the last decade of available data and the closest to our period) was 0.7% for anthropogenic sources but 19% for BB sources (4% and 19%, respectively, without the detrending). Furthermore, the areas that we identify as hot spots of constituents' IAV are typically away from anthropogenic sources (mainly in tropical South America, equatorial Asia, and boreal forest regions), which implies that even if realistic, interannually varying anthropogenic emissions had been used, the results would not be expected to change substantially.

We also note that for tropospheric ozone, the clearest and easier to explain IAV hot spots (over equatorial Asia and South America) appeared only in one season (NH autumn), with the rest of the seasons featuring IAV hot spots in an unexpectedly remote region (the western and central tropical Pacific Ocean). Furthermore, the role of biomass burning emissions in driving ozone IAV was not clear. This and the general disagreement between studies that have examined ozone IAV suggest that further investigation is needed to understand the magnitude of ozone IAV and its drivers. Nevertheless, we demonstrate that global composition-climate models can be used in conjunction with satellite information to shed light on this complicated topic. We also expect that the use of Earth system models that involve changes in and interactions between atmospheric composition, climate, and the biosphere, including fire activity, could shed more light on how such influences might change in a future climate.

Acknowledgments

The authors wish to thank NASA ACMAP for funding and the NASA High-End Computing (HEC) Program for computation resources through the NASA Center for Climate Simulation (NCCS) at Goddard Space Flight Center. Also, the authors thank the European Commission's Marie Curie International Research Staff Exchange Scheme (IRSES) for funding under the project titled "Regional climate-air quality interactions (REQUA)." M. Marlier would like to thank the National Science Foundation's Graduate Research Fellowship Program (NSF GRFP) for funding. The satellite and nonsatellite data sets used for this analysis are publicly available from the corresponding data set websites (TES: ftp://l5eil01.larc.nasa.gov/TES/, MODIS: http://modis-atmos.gsfc.nasa.gov/MOD08_M3/, MISR: https://eosweb.larc.nasa.gov/project/misr/version/pge12c, GMD: ftp://ftp.cmdl.noaa.gov/data/trace_gases/co/flask/, and WOUDC: http://beta.woudc.org/data/stations/, AERONET: http://aeronet.gsfc.nasa.gov/). All the model output data and the analysis codes used here are available for free from the lead author upon request (a.voulgarakis@imperial.ac.uk). We thank the TES, MODIS, MISR, GMD, WOUDC, and AERONET PIs and their staff for establishing and maintaining the websites used in this investigation.

References

Beer, R., T. A. Glavich, and D. M. Rider (2001), Tropospheric emission spectrometer for the Earth Observing System's Aura satellite, *Appl. Opt.*, *40*, 2356–2367.

Bian, H., and M. Prather (2002), Fast-J2 accurate simulations of photolysis in global climate models, *J. Atmos. Chem.*, *41*, 281–296.

Bowman, K. W., J. Worden, T. Steck, H. M. Worden, S. Clough, and C. Rodgers (2002), Capturing time and vertical variability of tropospheric ozone: A study using TES nadir retrievals, *J. Geophys. Res.*, *107*(D23), 4723, doi:10.1029/2002JD002150.

Bowman, K. W., et al. (2006), Tropospheric emission spectrometer: Retrieval method and error analysis, *IEEE Trans. Geosci. Remote. Sens.*, *44*, 1297–1307.

Bull, M., J. Matthews, D. McDonald, C. Moroney, S. Paradise, and M. Smyth (2009), MISR data products specifications, JPL. [Available at: https://eosweb.larc.nasa.gov/sites/default/files/project/misr/DPS_v50_RevR.pdf.]

Dalsøren, S. B., and I. S. A. Isaksen (2006), CTM study of changes in tropospheric hydroxyl distribution 1990–2001 and its impact on methane, *Geophys. Res. Lett.*, *33*, L23811, doi:10.1029/2006GL027295.

Duncan, B. N., R. V. Martin, A. C. Staudt, R. Yevich, and J. A. Logan (2003a), Interannual and seasonal variability of biomass burning emissions constrained by satellite observations, *J. Geophys. Res.*, *108*(D2), 4100, doi:10.1029/2002JD002378.

Duncan, B. N., I. Bey, M. Chin, L. J. Mickley, T. D. Fairlie, R. V. Martin, and H. Matsueda (2003b), Indonesian wildfires of 1997: Impact on tropospheric chemistry, *J. Geophys. Res.*, *108*(D15), 4458, doi:10.1029/2002JD003195.

Gery, M. W., G. Z. Whitten, J. P. Killus, and M. C. Dodge (1989), A photochemical kinetics mechanism for urban and regional scale computer modeling, *J. Geophys. Res.*, *94*, 925–956.

Giglio, L., J. T. Randerson, G. R. van der Werf, P. S. Kasibhatla, G. J. Collatz, D. C. Morton, and R. S. DeFries (2010), Assessing variability and long-term trends in burned area by merging multiple satellite fire products, *Biogeosciences*, *7*, 1171–1186, doi:10.5194/bg-7-1171-2010.

Guenther, A., et al. (1995), A global model of natural volatile organic compound emissions, *J. Geophys. Res.*, *100*, 8873–8892, doi:10.1029/94JD02950. [Available at http://www.agu.org/pubs/crossref/1995/94JD02950.shtml.]

Guenther, A., T. Karl, P. Harley, C. Wiedinmyer, P. I. Palmer, and C. Geron (2006), Estimates of global terrestrial isoprene emissions using MEGAN (Model of Emissions of Gases and Aerosols from Nature), *Atmos. Chem. Phys.*, *6*, 3181–3210, doi:10.5194/acp-6-3181-2006.

Habib, G., C. Venkataraman, I. Chiapello, S. Ramachandran, O. Boucher, and M. S. Reddy (2006), Seasonal and interannual variability in absorbing aerosols over India derived from TOMS: Relationship to regional meteorology and emissions, *Atmos. Environ.*, *40*, 1909–1921.

Hess, P., and N. Mahowald (2009), Interannual variability in hindcasts of atmospheric chemistry: The role of meteorology, *Atmos. Chem. Phys.*, *9*, 5261–5280, doi:10.5194/acp-9-5261-2009.

Holben, B. N., et al. (2001), An emerging ground-based aerosol climatology: Aerosol optical depth from AERONET, *J. Geophys. Res.*, *106*, 12,067–12,097, doi:10.1029/2001JD900014.

Houweling, S., F. Dentener, and J. Lelieveld (1998), The impact of non-methane hydrocarbon compounds on tropospheric photochemistry, *J. Geophys. Res.*, *103*, 10,673–10,696, doi:10.1029/97JD03582.

Huang, L., R. Fu, and J. H. Jiang (2014), Impacts of fire emissions and transport pathways on the interannual variation of CO in the tropical upper troposphere, *Atmos. Chem. Phys.*, *14*, 4087–4099, doi:10.5194/acp-14-4087-2014.

Jaffe, D. A., and N. L. Wigder (2012), Ozone production from wildfires: A critical review, *Atmos. Environ.*, *51*, 1–10, doi:10.1016/j.atmosenv.2011.11.063.

Ji, Y., and E. Stocker (2002), Seasonal, intraseasonal, and interannual variability of global land fires and their effects on atmospheric aerosol distribution, *J. Geophys. Res.*, *107*(D23), 4697, doi:10.1029/2002JD002331.

Kahn, R., et al. (2009), MISR aerosol product attributes and statistical comparisons with MODIS, *IEEE Trans. Geosci. Remote Sens.*, *47*(12, Part 2), 4095–4114.

Koch, D., G. A. Schmidt, and C. V. Field (2006), Sulfur, sea salt and radionuclide aerosols in GISS ModelE, *J. Geophys. Res.*, *111*, D06206, doi:10.1029/2004JD005550.

Koch, D., T. Bond, D. Streets, and N. Unger (2007), Linking future aerosol radiative forcing to shifts in source activities, *Geophys. Res. Lett.*, *34*, L05821, doi:10.1029/2006GL028360.

Koumoutsaris, S., I. Bey, S. Generoso, and V. Thouret (2008), Influence of El Niño–Southern Oscillation on the interannual variability of tropospheric ozone in the northern midlatitudes, *J. Geophys. Res.*, *113*, D19301, doi:10.1029/2007JD009753.

Lamarque, J.-F., et al. (2010), Historical (1850–2000) gridded anthropogenic and biomass burning emissions of reactive gases and aerosols: Methodology and application, *Atmos. Chem. Phys.*, *10*, 7017–7039, doi:10.5194/acp-10-7017-2010.

Lathiere, J., D. A. Hauglustaine, A. D. Friend, N. De Noblet-Ducoudre, N. Viovy, and G. A. Folberth (2006), Impact of climate variability and land use changes on global biogenic volatile organic compound emissions, *Atmos. Chem. Phys.*, *6*, 2129–2146.

Li, J., B. E. Carlson, and A. A. Lacis (2014), Application of spectral analysis techniques in the inter-comparison of aerosol data, Part II: Using maximum covariance analysis to effectively compare spatio-temporal variability of satellite and AERONET measured aerosol optical depth, *J. Geophys. Res. Atmos.*, *119*, 153–166, doi:10.1002/2013JD020537.

Lin, M., L. W. Horowitz, S. J. Oltmans, A. M. Fiore, and S. Fan (2014), Tropospheric ozone trends at Manna Loa Observatory tied to decadal climate variability, *Nat. Geosci.*, *7*, 136–143, doi:10.1038/NGEO2066.

Logan, J. A., I. Megretskaia, R. Nassar, L. T. Murray, L. Zhang, K. W. Bowman, H. M. Worden, and M. Luo (2008), Effects of the 2006 El Nino on tropospheric composition as revealed by data from the Tropospheric Emission Spectrometer (TES), *Geophys. Res. Lett.*, *35*, L03816, doi:10.1029/2007GL031698.

Lopez, J. P., M. Luo, L. E. Christensen, M. Loewenstein, H. Jost, C. R. Webster, and G. Osterman (2008), TES carbon monoxide validation during two AVE campaigns using the Argus and ALIAS instruments on NASA's WB-57F, *J. Geophys. Res.*, *113*, D16S47, doi:10.1029/2007JD008811.

Luo, M., et al. (2007), TES carbon monoxide validation with DACOM aircraft measurements during INTEX-B 2006b, *J. Geophys. Res.*, *112*, D24S48, doi:10.1029/2007JD008803.

Marlier, M. E., R. S. DeFries, A. Voulgarakis, P. L. Kinney, J. T. Randerson, D. T. Shindell, Y. Chen, and G. Faluvegi (2013), El Niño and health risks from landscape fire emissions in southeast Asia, *Nat. Clim. Change*, *3*, 131–136, doi:10.1038/nclimate1658.

Mészáros, T., L. Haszpra, and A. Gelencsér (2005), Tracking changes in carbon monoxide budget over Europe between 1995 and 2000, *Atmos. Environ.*, *39*, 7297–7306.

Monks, S. A., S. R. Arnold, and M. P. Chipperfield (2012), Evidence for El Niño-Southern Oscillation (ENSO) influence on Arctic CO interannual variability through biomass burning emissions, *Geophys. Res. Lett.*, *39*, L14804, doi:10.1029/2012GL052512.

Montzka, S. A., M. Krol, E. Dlugokencky, B. Hall, P. Jöckel, and J. Lelieveld (2011), Small interannual variability of global atmospheric hydroxyl, *Science*, *331*, 67, doi:10.1126/science.1197640.

Mu, Q., and H. Liao (2014), Simulation of the interannual variations of aerosols in China: Role of variations in meteorological parameters, *Atmos. Chem. Phys.*, *14*, 9597–9612, doi:10.5194/acp-14-9597-2014.

Neu, J. L., T. Flury, G. L. Manney, M. L. Santee, N. J. Livesey, and J. Worden (2014), Tropospheric ozone variations governed by changes in stratospheric circulation, *Nat. Geosci.*, *7*, 340–344, doi:10.1038/ngeo2138.

Novelli, P. C., and K. A. Masarie (2010), Atmospheric carbon monoxide dry air mole fractions from the NOAA ESRL carbon cycle cooperative global air sampling network, 1988–2009, Version: 2011-10-14. [Available at ftp://ftp.cmdl.noaa.gov/data/trace_gases/co/flask/, last access: 5 March 2015.]

Oman, L. D., A. R. Douglass, J. R. Ziemke, J. M. Rodriguez, D. W. Waugh, and J. E. Nielsen (2013), The ozone response to ENSO in Aura satellite measurements and a chemistry-climate simulation, *J. Geophys. Res. Atmos.*, *118*, 965–976, doi:10.1029/2012JD018546.

Osterman, G. B., et al. (2008), Validation of Tropospheric Emission Spectrometer (TES) measurements of the total, stratospheric, and tropospheric column abundance of ozone, *J. Geophys. Res.*, *113*, D15S16, doi:10.1029/2007JD008801.

Philander, S. G. H. (1990), *El Niño, La Niña and the Southern Oscillation*, 289 pp., Academic Press, San Diego, Calif.

Price, C., J. Penner, and M. Prather (1997), NO_x from lightning, 1, global distribution based on lightning physics, *J. Geophys. Res.*, *102*, 5929–5941, doi:10.1029/96JD03504.

Putero, D., T. C. Landi, P. Cristofanelli, A. Marinoni, P. Laj, R. Duchi, F. Calzolari, G. P. Verza, and P. Bonasoni (2014), Influence of open vegetation fires on black carbon and ozone variability in the southern Himalayas (NCO-P, 5079 m a.s.l.), *Environ. Pollut.*, *184*, 597–604.

Randerson, J. T., G. R. van der Werf, G. J. Collatz, L. Giglio, C. J. Still, P. Kasibhatla, J. B. Miller, J. W. C. White, R. S. DeFries, and E. S. Kasischke (2005), Fire emissions from C3 and C4 vegetation and their influence on interannual variability of atmospheric CO_2 and $\delta^{13}CO_2$, *Global Biogeochem. Cycles*, *19*, GB2019, doi:10.1029/2004GB002366.

Remer, L. A., et al. (2005), The MODIS aerosol algorithm, products, and validation, *J. Atmos. Sci.*, *62*, 947–973.

Richards, N. A. D., G. B. Osterman, E. V. Browell, J. W. Hair, M. Avery, and Q. Li (2008), Validation of Tropospheric Emission Spectrometer ozone profiles with aircraft observations during the Intercontinental Chemical Transport Experiment-B, *J. Geophys. Res.*, *113*, D16S29, doi:10.1029/2007JD008815.

Rodgers, C. D. (2000), *Inverse Methods for Atmospheric Sounding: Theory and Practice*, World Sci, Hackensack, N. J.

Savage, N. H., J. A. Pyle, P. Braesicke, F. Wittrock, A. Richter, H. Nuß, J. P. Burrows, M. G. Schultz, T. Pulles, and M. van het Bolscher (2008), The sensitivity of Western European NO_2 columns to interannual variability of meteorology and emissions: A model-GOME study, *Atmos. Sci. Lett.*, *9*(4), 182–188, doi:10.1002/asl.193.

Schmidt, G. A., et al. (2014), Configuration and assessment of the GISS ModelE2 contributions to the CMIP5 archive, *J. Adv. Model. Earth Syst.*, *6*(1), 141–184, doi:10.1002/2013MS000265.

Schultz, M. G., A. Heil, J. J. Hoelzemann, A. Spessa, K. Thonicke, J. G. Goldammer, A. C. Held, J. M. C. Pereira, and M. van het Bolscher (2008), Global wildland fire emissions from 1960 to 2000, *Global Biogeochem. Cycles*, *22*, GB2002, doi:10.1029/2007GB003031.

Shindell, D. T., et al. (2013), Interactive ozone and methane chemistry in GISS-E2 historical and future climate simulations, *Atmos. Chem. Phys.*, *13*, 2653–2689, doi:10.5194/acp-13-2653-2013.

Spichtinger, N., R. Damoah, S. Eckhardt, C. Forster, P. James, S. Beirle, T. Marbach, T. Wagner, P. C. Novelli, and A. Stohl (2004), Boreal forest fires in 1997 and 1998: a seasonal comparison using transport model simulations and measurement data, *Atmos. Chem. Phys.*, *4*, 1857–1868, doi:10.5194/acp-4-1857-2004.

Spracklen, D. V., J. A. Logan, L. J. Mickley, R. J. Park, R. Yevich, A. L. Westerling, and D. A. Jaffe (2007), Wildfires drive interannual variability of organic carbon aerosol in the western U.S. in summer, *Geophys. Res. Lett.*, *34*, L16816, doi:10.1029/2007GL030037.

Stockwell, W. R., F. Kirchner, M. Kuhn, and S. Seefeld (1997), A new mechanism for regional atmospheric chemistry modeling, *J. Geophys. Res.*, *102*, 25,847–25,879, doi:10.1029/97JD00849.

Strode, S. A., and S. Pawson (2013), Detection of carbon monoxide trends in the presence of interannual variability, *J. Geophys. Res. Atmos.*, *118*, 12,257–12,273, doi:10.1002/2013JD020258.

Szopa, S., D. A. Hauglustaine, and P. Ciais (2007), Relative contributions of biomass burning emissions and atmospheric transport to carbon monoxide interannual variability, *Geophys. Res. Lett.*, *34*, L18810, doi:10.1029/2007GL030231.

Tsigaridis, K., and M. Kanakidou (2007), Secondary organic aerosol importance in the future atmosphere, *Atmos. Environ.*, *41*, 4682–4692, doi:10.1016/j.atmosenv.2007.03.045.

Uno, I., et al. (2007), Systematic analysis of interannual and seasonal variations of model-simulated tropospheric NO2 in Asia and comparison with GOME-satellite data, *Atmos. Chem. Phys.*, *7*, 1671–1681, doi:10.5194/acp-7-1671-2007.

van der Werf, G. R., J. T. Randerson, L. Giglio, G. J. Collatz, M. Mu, P. S. Kasibhatla, D. C. Morton, R. S. DeFries, Y. Jin, and T. T. van Leeuwen (2010), Global fire emissions and the contribution of deforestation, savanna, forest, agricultural, and peat fires (1997–2009), *Atmos. Chem. Phys.*, *10*, 11,707–11,735, doi:10.5194/acp-10-11707-2010.

Verstraeten, W. W., K. F. Boersma, J. Zörner, M. A. F. Allaart, K. W. Bowman, and J. R. Worden (2013), Validation of six years of TES tropospheric ozone retrievals with ozonesonde measurements: Implications for spatial patterns and temporal stability in the bias, *Atmos. Meas. Tech.*, *6*, 1413–1423, doi:10.5194/amt-6-1413-2013.

Voulgarakis, A., and R. Field (2015), Fire influences on atmospheric composition, air quality, and climate, *Curr. Pollut. Rep.*, doi:10.1007/s40726-015-0007-z.

Voulgarakis, A., N. H. Savage, O. Wild, P. Braesicke, P. J. Young, G. D. Carver, and J. A. Pyle (2010), Interannual variability of tropospheric composition: The influence of changes in emissions, meteorology and clouds, *Atmos. Chem. Phys.*, *10*, 2491–2506, doi:10.5194/acp-10-2491-2010.

Voulgarakis, A., P. J. Telford, A. M. Aghedo, P. Braesicke, G. Faluvegi, N. L. Abraham, K. W. Bowman, J. A. Pyle, and D. T. Shindell (2011a), Global multi-year O_3-CO correlation patterns from models and TES satellite observations, *Atmos. Chem. Phys.*, *11*, 5819–5838, doi:10.5194/acp-11-5819-2011.

Voulgarakis, A., P. Hadjinicolaou, and J. A. Pyle (2011b), Increases in global tropospheric ozone following an El Niño event: Examining stratospheric ozone variability as a potential driver, *Atmos. Sci. Lett.*, *12*, 228–232.

Ward, D. S., S. Kloster, N. M. Mahowald, B. M. Rogers, J. T. Randerson, and P. G. Hess (2012), The changing radiative forcing of fires: Global model estimates for past, present and future, *Atmos. Chem. Phys.*, *12*, 10,857–10,886, doi:10.5194/acp-12-10857-2012.

Wild, O., and P. I. Palmer (2008), How sensitive is tropospheric oxidation to anthropogenic emissions?, *Geophys. Res. Lett.*, *35*, L22802, doi:10.1029/2008GL035718.

Wild, O., X. Zhu, and M. J. Prather (2000), Fast-J accurate simulation of in- and below-cloud photolysis in global chemical models, *J. Atmos. Chem.*, *37*, 245–282, doi:10.1023/A:1006415919030.

Yoon, J., J. P. Burrows, M. Vountas, W. von Hoyningen-Huene, D. Y. Chang, A. Richter, and A. Hilboll (2014), Changes in atmospheric aerosol loading retrieved from space-based measurements during the past decade, *Atmos. Chem. Phys.*, *14*, 6881–6902, doi:10.5194/acp-14-6881-2014.

Zbinden, R. M., V. Thouret, P. Ricaud, F. Carminati, J.-P. Cammas, and P. Nédélec (2013), Climatology of pure tropospheric profiles and column contents of ozone and carbon monoxide using MOZAIC in the mid-northern latitudes (24°N to 50°N) from 1994 to 2009, *Atmos. Chem. Phys.*, *13*, 12,363–12,388, doi:10.5194/acp-13-12363-2013.

Zeng, G., and J. A. Pyle (2005), Influence of El Niño Southern Oscillation on stratosphere/troposphere exchange and the global tropospheric ozone budget, *Geophys. Res. Lett.*, *32*, L01814, doi:10.1029/2004GL021353.

Zhao, T. L., S. L. Gong, P. Huang, and D. Lavoué (2012), Hemispheric transport and influence of meteorology on global aerosol climatology, *Atmos. Chem. Phys.*, *12*, 7609–7624, doi:10.5194/acp-12-7609-2012.